Earth and Space Science

RESEARCH ARTICLE
10.1029/2018EA000436

Improving Near-Surface Retrievals of Surface Humidity Over the Global Open Oceans From Passive Microwave Observations

J. Brent Roberts[1], C. A. Clayson[2], and F. R. Robertson[1]

[1]NASA Marshall Space Flight Center, Huntsville, AL, USA, [2]Woods Hole Oceanographic Institution, Falmouth, MA, USA

Key Points:
- Current remote sensing estimates of ocean surface humidity exhibit large-scale and spatially coherent biases
- These biases are organized at the regional scale by atmospheric dynamics that control the vertical structure of water vapor and cloud amount
- Analyses show that state-dependent bias corrections can be developed to result in more consistent ocean surface humidity estimates

Correspondence to:
J. B. Roberts,
jason.b.roberts@nasa.gov

Citation:
Roberts, J. B., Clayson, C. A., & Robertson, F. R. (2019). Improving near-surface retrievals of surface humidity over the global open oceans from passive microwave observations. *Earth and Space Science*, *6*, 1220–1233. https://doi.org/10.1029/2018EA000436

Received 14 SEP 2018
Accepted 4 JUN 2019
Accepted article online 25 JUN 2019
Published online 22 JUL 2019

Abstract Ocean evaporative fluxes are a critical component of the Earth's energy and water cycle, but their estimation remains uncertain. Near-surface humidity is a required input to bulk flux algorithms that relate mean surface values to the turbulent fluxes. Several satellite-derived turbulent flux products have been developed over the last decade that utilize passive microwave imager observations to estimate the surface humidity. It is known, however, that these estimates tend to diverge from one another and from in situ observations. Analysis of current state-of-the-art satellite estimates provided herein reveals that regional-scale biases in these products remain significant. Investigations reveal a link between the spatial coherency of the observed biases to atmospheric dynamical controls of water vapor vertical stratification, cloud liquid water, and sea surface temperature. This information is used to develop a simple state-dependent bias correction that results in more consistent ocean surface humidity estimates. A principal conclusion is that further improvements to ocean near-surface humidity estimation using microwave radiometers requires incorporation of prior information on water vapor stratification and sea surface temperature.

Plain Language Summary To reduce the uncertainties in ocean evaporation—which is currently of leading order in water and energy budget studies—progress is necessary to understand the sources of error in the surface measurements needed to model the ocean-atmosphere exchange of water. Recent studies have independently demonstrated systematic uncertainties in estimates of ocean evaporation and surface humidity related to large-scale dynamics and vertical water vapor stratification. The results presented herein directly establish the link between the large-scale patterns of uncertainties in ocean evaporation estimates and the sources of errors in estimation of surface humidity from remote sensing observations. These results are used to characterize the relationship of surface humidity errors to physical quantities—sea surface temperature, water vapor stratification, and cloudiness—that are used to develop simple corrections for these errors. While effective, these corrections indicate the need for future algorithm development that incorporates information on these conditions directly into the remote sensing inverse-modeling process.

1. Introduction

Ocean evaporation and its associated latent heat flux are critical components of the Earth's energy and water balance. Recent investigations by Rodell et al. (2015) and L'Ecuyer et al. (2015) have demonstrated that the uncertainty in the estimates of turbulent exchange of moisture across the ocean interface is of leading order with respect to uncertainties in global atmospheric water and energy budgets. Ocean evaporation has historically been estimated through application of "bulk flux" algorithms that relate mean near-surface meteorology—surface skin and air temperature, wind speed, and air humidity—to the turbulent sensible and latent heat fluxes (Fairall et al., 2003; Large & Pond, 1982). Intercomparison studies have been performed that indicate uncertainties with each component; Brunke et al. (2011) note significant regional variability in the *Q*air biases. Estimates of *Q*air are available from in situ observations including buoys and voluntary observing ships (VOS), from satellite retrievals and by model reanalyses. Surface observations are limited in space and time over the global oceans; Berry and Kent (2016) and Gulev et al. (2007) discuss sampling issues related to direct ocean surface observations with the former noting a 20% reduction in global coverage since the early 1990s. Reanalyses may address issues related to poor sampling, but they are subject to changes in the observing system that inject artificial variability into long-term estimates (Roberts et al., 2012; Robertson et al., 2014). Josey et al. (2014) find that assimilation of surface observations from moored buoys remains

problematic in reanalyses. Further, differences of 0.5–1.0 g/kg remain for *Q*air seasonal to annual means between reanalysis estimates that are large enough to, alone, preclude closing the surface energy budget to within the oft-stated goal of 10 W/m^2 (Kent et al., 2014).

Microwave imagers are designed to measure precipitation, integrated water vapor and liquid water content, sea surface temperature (SST), and wind speed. While lacking strong direct sensitivity to the near-surface thermodynamic state, retrievals of surface air humidity have successfully been made using regression-based approaches. These approaches stem from the early work by Liu (1986) that highlights the strong connection between columnar water vapor and *Q*air on monthly time scales and the more instantaneous connection of lower layer boundary moisture (e.g., within the lowest 500 m) to *Q*air discussed in Schulz et al. (1993). Wentz (1997) has also noted that coarse water vapor profile information is contained within the microwave imager channels. The physical mechanism is related to pressure-induced broadening and narrowing of water vapor absorption lines. This sensitivity, though limited, has provided the foundation for microwave imager-based estimates of *Q*air (Bentamy et al., 2003, 2013; Chou et al., 1995, 1997; Roberts et al., 2010; Schlüssel et al., 1995; Schulz et al., 1993; Tomita et al., 2018). These algorithms rely on similar sets of input brightness temperatures from satellite microwave imagers; they differ through choice and sampling of training data sets, regression algorithms (i.e., linear vs. nonlinear), and inclusion of externally specified predictors. Studies such as Prytherch et al. (2014) that have intercompared these approaches find annual mean differences exceeding 1 g/kg and regional monthly mean differences of 2 g/kg. Further, they find monthly mean biases against surface observations that exhibit strong regional coherence; these regional variations were also noted in direct comparisons to research vessel observations in Brunke et al. (2011).

Recent intercomparisons of ocean evaporation estimates from satellite products have been performed within the context of dynamical regimes related to the columnar water budget (Wong & Behrangi, 2018). The intent of their decomposition, as discussed in Wong et al. (2016), is to better connect the large-scale dynamics to moisture convergence variability. Specifically, it decomposes moisture convergence into convergent and advective components to define a "water-budget-phase-space" with regimes where total moisture convergence (or divergence) are driven primarily by convergence, advection, or their combination. In addition to being used to examine moisture convergence variability across models and reanalyses (see Wong et al., 2016), Wong and Behrangi (2018) demonstrate how these dynamical regimes effectively partition interproduct evaporation differences relative to columnar moisture convergence and divergence at daily time scales. It is important to recognize that the evaporation differences should be related to differences in the near-surface bulk variables between products. In this study, our principal motivation is to connect the regime-dependent evaporation uncertainties observed in Wong and Behrangi (2018) to the regionally coherent patterns of surface humidity biases illustrated in Prytherch et al. (2014). We further discuss how these biases arise relative to the underlying satellite retrievals used to estimate *Q*air. A simple, yet effective state-dependent bias correction is developed that harmonizes many of the current retrieval estimates.

2. Data

2.1. Satellite Estimates

There are multiple satellite-derived latent heat flux products developed through use of observations from the seven-channel ($19_{v,h}$ GHz, 22_{v} GHz, $37_{v,h}$ GHz, $85_{v,h}$ GHz; v/h denotes polarization) Special Sensor Microwave/Imager and related sensors. We examine a total of six modern *Q*air estimates available from the following products: JOFURO (Japanese Ocean Flux Data Sets with Use of Remote Sensing Observations) including versions 2 (Tomita et al., 2010) and 3 (Tomita et al., 2018); GSSTF (Goddard Satellite-based Surface Turbulent Fluxes) version 3 (Shie, 2014); HOAPS (Hamburg Ocean Atmosphere Parameters and Fluxes from Satellite) version 3.2 (Andersson et al., 2010); IFREMER (Institut Français pour la Recherche et l'Exploitation de la MER) version 4 (Bentamy et al., 2017); and the SEAFLUX-Climate Data Record version 2 (Clayson, 2016). Collectively, these products are divided into those whose *Q*air algorithms use only microwave brightness temperatures—JOFUROv2, GSSTFv3, and HOAPSv3.2—and those that include a priori information on water vapor stratification (JOFUROv3), SST (IFREMERv4 and SEAFLUXv2), and cloud liquid water (SEAFLUXv2). Data are evaluated over the 55°N to 55°S open ocean (i.e., ice-free) domain as these satellite products are unable to provide estimates over sea ice. Table 1 provides the functional formulation of each of the data products considered in this study.

Table 1
Algorithm Description by Product

Product	Algorithm	Details
JOFUROv2	$Q\text{air} = a_0 + \sum_{i=1}^{n=5} a_i T_i$	i: [19_v, 19_h, 22_v, 37_v, 37_h] *Least squares*[a]
GSSTFv3	$Q\text{air} = a_0 + \sum_{i=1}^{n=4} a_i T_i$	i: [19_v, 19_h, 22_v, 37_v] *Least squares*
HOAPSv3.2	$Q\text{air} = a_0 + \sum_{i=1}^{n=4} a_i T_i$	i: [19_v, 19_h, 22_v, 37_v] *Least squares*
JOFUROv3	$Q\text{air} = a_0 + \sum_{i=1}^{n=7} a_i T_i + \sum_{k=1}^{n=3} b_k (T_k)^2 + cQ$	i: [19_v, 19_h, 22_v, 37_v, 37_h, 85_v, 85_h] k: [22_v, 85_v, 85_h] a_i, b_k, c: trained for six ranges of water vapor scale height; *Least squares*
IFREMERv4	$Q\text{air} = F_{\text{ML}}(T_i, \text{SST}, \text{SST} - T\text{air})$	i: [19_v, 19_h, 22_v, 37_v] *Maximum-likelihood*
SEAFLUXv2	$Q\text{air} = F_{\text{NN}}(T_i, \text{SST}, \text{LWP})$	i: [19_v, 19_h, 22_v, 37_v, 37_h, 85_v, 85_h] *Neural network*

Note. LWP = liquid water path; NN = neural network; SST = sea surface temperature; GSSTFv3 = Goddard Satellite-based Surface Turbulent Fluxes version 3; HOAPSv3.2 = Hamburg Ocean Atmosphere Parameters and Fluxes from Satellite version 3.2; IFREMERv4 = Institut Français pour la Recherche et l'Exploitation de la MER version 4; JOFUROv2 = Japanese Ocean Flux Data Sets with Use of Remote Sensing Observations version 2.
[a]Denotes the type of algorithms used to train regression function.

JOFUROv2 applies the five-channel regression of Schlüssel et al. (1995), while both GSSTFv3 and HOAPSv3.2 apply the four-channel regression of Bentamy et al. (2003) that follows from Schulz et al. (1993). JOFUROv3 applies a seven-channel retrieval but also includes a priori estimates of columnar water vapor, Q, and uses coefficients tuned for six different categories of water vapor stratification represented by the water vapor scale height (see Tomita et al., 2018). JOFUROv3 also includes quadratic terms for the 22_v, 85_v, and 85_h channel. Each of the above formulations uses least squares regression to estimate model coefficients. IFREMERv4 applies a maximum-likelihood procedure discussed in Bentamy et al. (2013) as an extension of their 2003 approach but which includes external information on SST and surface stability indicated by differences in the sea surface and 10-m air temperature (Tair). SEAFLUXv2 applies the Roberts et al. (2010) seven-channel nonlinear neural network regression that includes specified estimates of SST and liquid water path (LWP). The latter two algorithms were developed upon noting SST-dependent biases in brightness-temperature-only regressions. While SST and Qair are highly correlated, atmospheric variability—including that related to columnar water vapor—significantly impacts the observed microwave brightness and thus Qair estimates do not remain completely dependent upon the SST alone. Similar results were found through inclusion of SST in an Advanced Microwave Sounding Unit retrieval of air temperature in Jackson and Wick (2010); that is, atmospheric variations impacting the observed microwave brightness impart independent information. Without the SST information—which sets a baseline for the background surface emission—the retrievals using only the radiometer channels are forced to model the functional variations between the microwave observations and atmospheric state in terms of atmospheric variability alone. All products are available during the common period 1992–2008 and each was resampled to a common 1° by 1°, daily average grid using a conservative remapping (Jones, 1999) technique. All Qair estimates are represented at a standard height of 10 m.

2.2. Surface Observations

As a source for evaluation of the satellite estimates, direct surface observations are available from multiple platforms including drifting and moored buoys, as well as VOS. A large collection of this data has been organized and evaluated to support the development of the National Oceanography Centre, Southampton (NOCS) Flux Dataset version 2 (Berry & Kent, 2009). Development of this surface observation-based data set included performing bias adjustments to humidity observations related to measurement techniques and use of VOS metadata records to standardize all data to a common 10-m reference height. After adjustments, a 0.2-g/kg bias uncertainty of these estimates remains (Berry & Kent, 2011). While NOCSv2 is

developed as a monthly product, we utilize their daily corrected input fields—available on the same 1° by 1° grid as the satellite estimates—for evaluation of the satellite-derived *Q*air estimates. These daily fields include uncertainty estimates due to random and sampling errors. Independent comparisons with the instantaneous VOS data used in constructing the daily fields reveal that daily pixels containing at least one direct observation were associated with random uncertainty estimates less than 1.5 g/kg, and thus, we only keep the NOCSv2 daily pixels having estimated errors below this threshold. This choice has little impact on the systematic uncertainties evaluated herein. These daily average estimates have been collocated with those from each of the satellite products and used to assess the sign, strength, and spatial patterns of systematic errors for each data set.

2.3. Reanalysis

The water-budget-based dynamical decomposition of Wong et al. (2016) relies on estimates of vertically integrated moisture transport and *Q*. Following their study, we obtain the required fields from the recently produced Modern-Era Retrospective Analysis for Research and Applications version 2 (MERRA-2, Gelaro et al., 2017). Further, we obtain vertically integrated cloud liquid water and SSTs from MERRA-2 to assist evaluating the satellite product *Q*air biases.

3. Methods

3.1. Dynamical Regimes

Following Wong and Behrangi (2018), the conservation equation for column-integrated water vapor can be written as follows:

$$\frac{\partial Q}{\partial t} + P - E = -\nabla\cdot\left(Q\widetilde{\boldsymbol{V}}\right) = -\widetilde{\boldsymbol{V}}\cdot\nabla Q - Q\nabla\cdot\widetilde{\boldsymbol{V}} = Q_{\mathrm{adv}} + Q_{\mathrm{con}} \tag{1}$$

where P and E are surface precipitation and evaporation, respectively;

$$\widetilde{\boldsymbol{V}} = \frac{1}{Q}\int_0^{P_{\mathrm{sfc}}} q\boldsymbol{v}\frac{\mathrm{d}p}{g} \tag{2}$$

is the column-integrated moisture transport vector scaled by precipitable water and q and $\boldsymbol{v}$ are the specific humidity and velocity. Equation (1) presents a decomposition of the total moisture convergence into an advective term, Q_{adv}, and the other term, Q_{con}, related to mass convergence (scaled by Q). Alternative decompositions of the vertically integrated moisture convergence could be made using an alternative scalar to that of Q. With the use of Q, $\widetilde{\boldsymbol{V}}$ can be interpreted as the water vapor weighted integral of winds. This choice results in an analysis that emphasizes advection related to gradients of total columnar moisture and a convergent component of lower layer winds as water vapor (and hence its weighting in $\widetilde{\boldsymbol{V}}$) decreases rapidly from the surface. Wong et al. (2016) demonstrate partitioning of total moisture convergence into this two-parameter space results in large-scale patterns where different "regimes"—as defined by different thresholds in $Q_{\mathrm{adv}}/Q_{\mathrm{con}}$ space—frequently occur. A total of nine dynamical regimes is identified in Wong et al. (2016) that represent the mixed conditions of strongly negative (−), neutral (0), and strongly positive (+) Q_{adv} and Q_{con}. Their analyses showed decomposition in this parameter space delineated regimes where the advective versus convergent components dominated, or were mixed, and that they align to well-known climatological patterns (e.g., tropical convergence zones, trade winds, and extratropical storm tracks) as well as succinctly partition several thermodynamic metrics (e.g., convective available potential energy, convective inhibition). As an example, they find the neutral Q_{adv} but strongly positive Q_{con} dynamical regime, A0C+, is constrained geographically to the tropics and more specifically to the Intertropical and South Pacific Convergence Zones. We have largely followed their regime definitions, but we have slightly modified their thresholds so that the near-neutral conditions rely on a threshold of 3 mm/day rather than 1 mm/day. We examined several similar thresholds, and none significantly impacts the qualitative results presented. This threshold was chosen as it appears to more accurately capture the position of the trade wind inversion within the two-parameter space.

3.2. State Dependence and Bias Corrections

Though most regression algorithms attempt to minimize the underlying squared error of the prediction, there remains a distinct possibility for state-dependent (i.e., conditional) biases to exist as related to

important but unaccounted for independent parameters. In this study, we demonstrate that the large-scale dynamical conditions organize the biases into spatially coherent patterns; however, the fundamental drivers of the retrieval errors are only indirectly related to the dynamics. The biases are driven directly by systematic deviations in the water vapor stratification, SST, and LWP from those conditions represented in the empirical training data sets. That is, the microwave brightness is not responding directly to dynamical advection and/or total convergence but to the profiles of water vapor, temperature, and clouds associated with that variability that alters the microwave radiative transfer. In this study, we demonstrate evidence of conditional biases related to these parameters and develop an a posteriori correction using a look-up table for the biases conditioned upon MERRA-2 estimated SST, precipitable water fraction ($^{Q_{900}}/_{Q}$), and columnar LWP. The precipitable water fraction is the relative abundance of water vapor integrated over the surface to 900 hPa, Q_{900}, to the total columnar water vapor. We partition the precipitable water fraction in 2.5% increments from 0% to 100%, SST in 2 °C increments from −2 °C to 34 °C, and cloud liquid water in 5-g/m^2 increments from 0 to 600 g/m^2. For each product all daily, collocated satellite-surface observation product differences are collected within each hypercube in this space and the mean bias is estimated. Given our large data set of observations, there are approximately 320 samples per bin (median of all bins across products) in this 3-D space. Bias corrections for each product are estimated using a trilinear interpolation of the contemporaneous daily estimates of $^{Q_{900}}/_{Q}$, SST, and LWP from MERRA-2 and added to each product. Several discretization sizes were tested with little impact. Further, we note that the primary objective is not to develop a definitive correction procedure but rather to illustrate the potential reduction of interproduct errors and differences if these additional parameters are better accounted for within the retrieval process.

4. Results and Discussion

Systematic errors are estimated as the mean difference of the collocated product and observed surface observations of *Q*air. Figure 1 illustrates these errors for each of the products assessed in this study; Figures 1a, 1c, and e are those algorithms relying on microwave brightness temperature-only (TB-only) regressions while those in Figures 1b, 1d, and 1f use regressions that include some additional a priori information (i.e., SST and water vapor scale height). Two contours are additionally overlain in each plot; blue and red contours indicate where the relative frequency of occurrence exceeds 15% (results are qualitatively similar for other contour choices) for the deep convective regime (A0C+) and the subtropical stable boundary layer (A0C−) regime, respectively. One immediately recognizes a strong correspondence between the large-scale coherent biases observed in each product, especially TB-only estimates, and the locations favored by these two regimes. The TB-only-based products either show significant overestimation of *Q*air in the A0C+ regimes (JOFUROv2) or significant underestimation of *Q*air in the A0C− regimes (GSSTFv3 and HOAPSv3.2), with biases exceeding 1.5 g/kg in amplitude; these are much larger than the estimated systematic uncertainty of 0.2 g/kg of the NOCSv2 surface observations. GSSTFv3 and HOAPSv3.2 use the same Bentamy et al. (2003) algorithm but are applied to separately intercalibrated and rain-flagged brightness temperature records. Thus, it appears these conditional errors stem primarily from the algorithm choice rather than the exact details of the intercalibrated imager data. Similar bias patterns are seen in the more recently developed algorithms but with amplitudes generally reduced to below 1 g/kg for the dry trade wind bias and less than 0.25 g/kg for the deep convective moist bias. JOFUROv3, compared to JOFUOv2, shows a remarkable reduction in the positive biases in the convective regimes; their newer algorithm differs through inclusion of water-vapor-scale-height information. However, this comes at the expense of introducing a potential dry bias in the northern Pacific and Atlantic. IFREMERv4—an update to the retrievals used in GSSTFv3 and HOAPSv3.2—has a reduced bias in the deep tropics but exhibits a moist bias of 0.3 g/kg over much of the ocean. SEAFLUXv2 has reduced biases in both the tropical convective and trade wind regimes compared to the TB-only algorithms. Both of these latter products include SST as an input but with no explicit information on water vapor stratification.

While Figure 1 is highly suggestive of an interplay between large-scale dynamical regimes (e.g., as noted by contours) and the observed *Q*air biases, we now seek to establish the connection between the retrieval physics and the dynamical regimes explicitly. Figure 2 demonstrates the partitioning of both lower layer precipitable water fraction and total LWP into the dynamical regimes spanned by Q_{con} and Q_{adv} parameter space. The nine dynamical regimes based on thresholds are also shown; areas above (below) the dashed line—Q_{con}

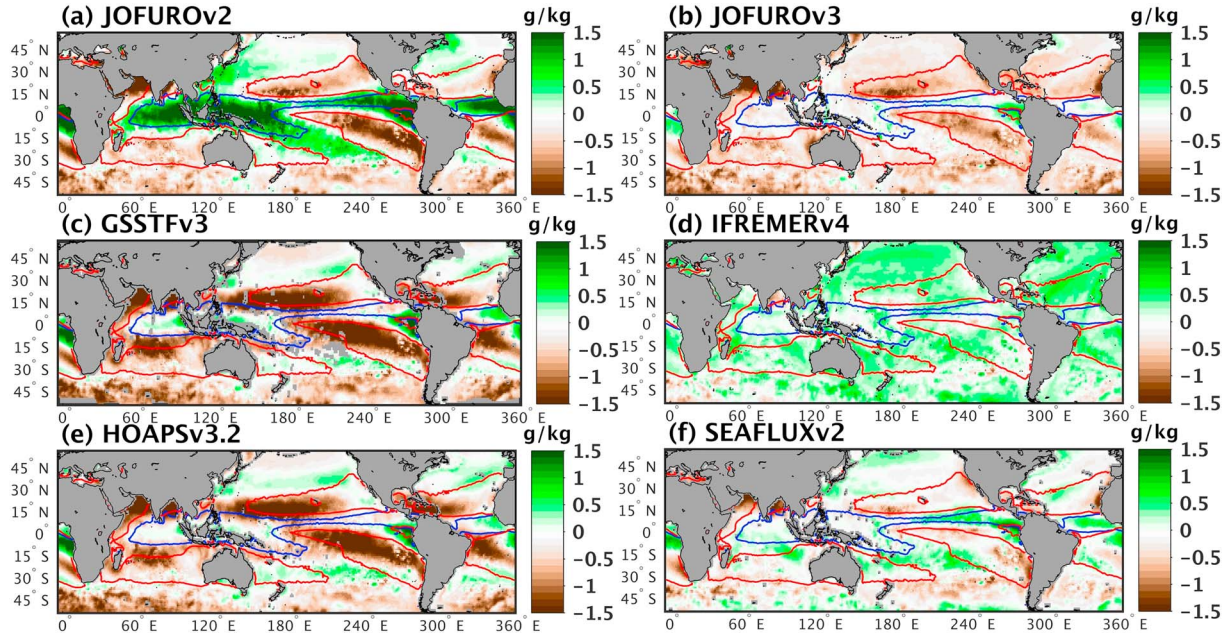

Figure 1. Mean differences (product minus observations) are shown for (a) JOFUROv2, (b) JOFUROv3, (c) GSSTFv3, (d) IFREMERv4, (e) HOAPSv3.2, and (f) SEAFLUXv2 over the common period 1992–2008 and open ocean domain (55°S to 55°N). Red (blue) contours outline the 15% relative frequency of occurrence regions for the subtropical inversion layer/A0C− (deep convective/A0C+) dynamical regimes. GSSTFv3 = Goddard Satellite-based Surface Turbulent Fluxes version 3; HOAPSv3.2 = Hamburg Ocean Atmosphere Parameters and Fluxes from Satellite version 3.2; IFREMERv4 = Institut Français pour la Recherche et l'Exploitation de la MER version 4; JOFUROv2 = Japanese Ocean Flux Data Sets with Use of Remote Sensing Observations version 2.

plus Q_{adv} equal to 0—represent total columnar moisture convergence (divergence). There is clearly strong variability in the lower layer water fraction associated with these regimes. In particular, the subtropical trade wind inversion A0C− regime exhibits very concentrated water vapor with fractional amounts greater than 60% found between the surface and 900 hPa. Conversely, the deep total moisture convergence regions (A0C+ and A+C+) are represented by deeply mixed water stratification. As may be expected, the total LWP shows strong variability aligned with the Q_{con} axis with LWP exceeding 0.2 mm in the most convergent regions.

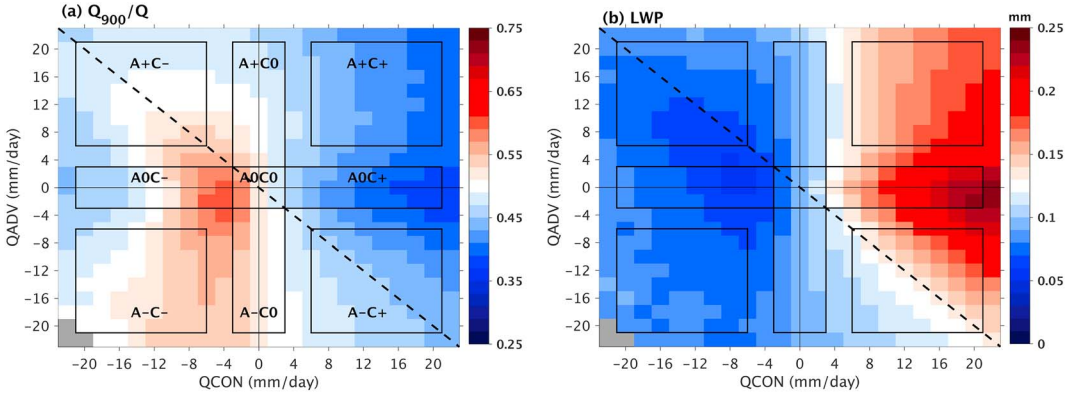

Figure 2. Composite binned mean conditions are shown for (a) water vapor fraction and (b) total liquid water path based on Modern-Era Retrospective Analysis for Research and Applications version 2 estimates within the two-parameter water budget decomposition into convective (Q_{con}) and advective (Q_{adv}) conditions. The dashed line separates total columnar moisture convergence (above) versus divergence (below); solid lines and labels are used to indicate the thresholds used to categorize the nine dynamical regimes tailoring the approach of Wong et al. (2016). Gray is used to indicate bins with less than 50 samples. LWP = liquid water path.

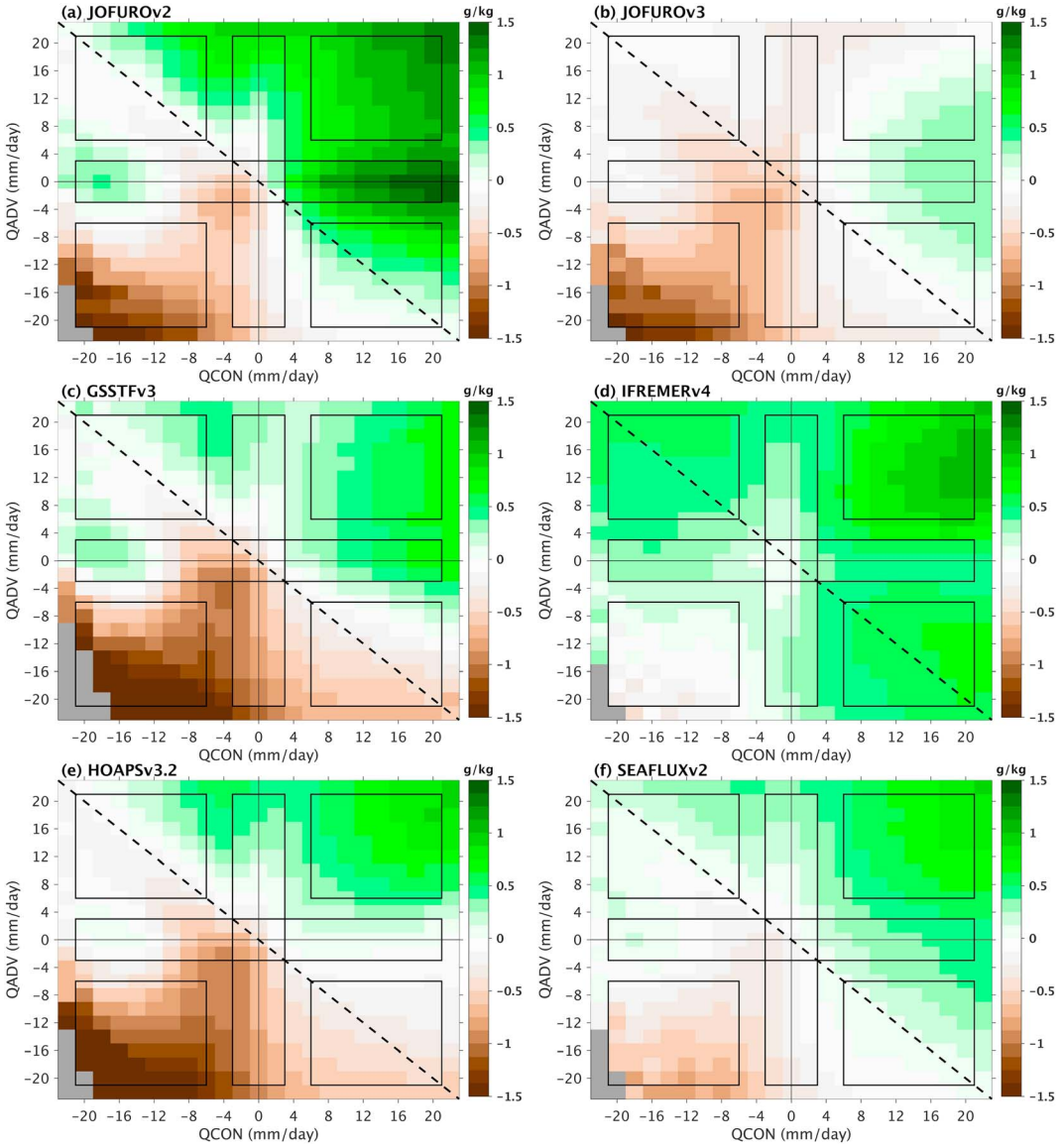

Figure 3. Composite binned mean differences are shown for (a) JOFUROv2, (b) JOFUROv3, (c) GSSTFv3, (d) IFREMERv4, (e) HOAPSv3.2, and (f) SEAFLUXv2 over the common period 1992–2008 within the two-parameter dynamical state space. Products that only use brightness temperature observations as algorithm inputs are in the left panels, while those including additional a priori inputs are organized in the right panels. GSSTFv3 = Goddard Satellite-based Surface Turbulent Fluxes version 3; HOAPSv3.2 = Hamburg Ocean Atmosphere Parameters and Fluxes from Satellite version 3.2; IFREMERv4 = Institut Français pour la Recherche et l'Exploitation de la MER version 4; JOFUROv2 = Japanese Ocean Flux Data Sets with Use of Remote Sensing Observations version 2.

Figure 3 illustrates the partitioning of the observed *Q*air biases into these same regimes for each product. To first order, the sign and strength of the satellite biases are organized above and below the diagonal line demarcating zones of total moisture convergence from divergence. However, there are local enhancements/deviations including changes in sign within this broader pattern. The TB-only regimes all exhibit a strong signature of moist biases in regions of total moisture convergence and dry biases in regions of total moisture divergence. JOFUROv2, GSSTFv3, and HOAPSv3.2 all also indicate a small positive bias in very divergent conditions (Q_{con} less than −16 mm/day) that corresponds to a local minimum in $^{Q_{900}}/_{Q}$ (see Figure 2a). JOFUROv3 exhibits a generally dry bias (0.2 to 0.5 g/kg) with little difference between regions of total moisture convergence/divergence excepting a small moist bias of 0.25 g/kg in the A0C+ regime. IFREMERv4 exhibits a moist bias of 0.3–0.5 g/kg across this phase space. SEAFLUXv2 exhibits a weak

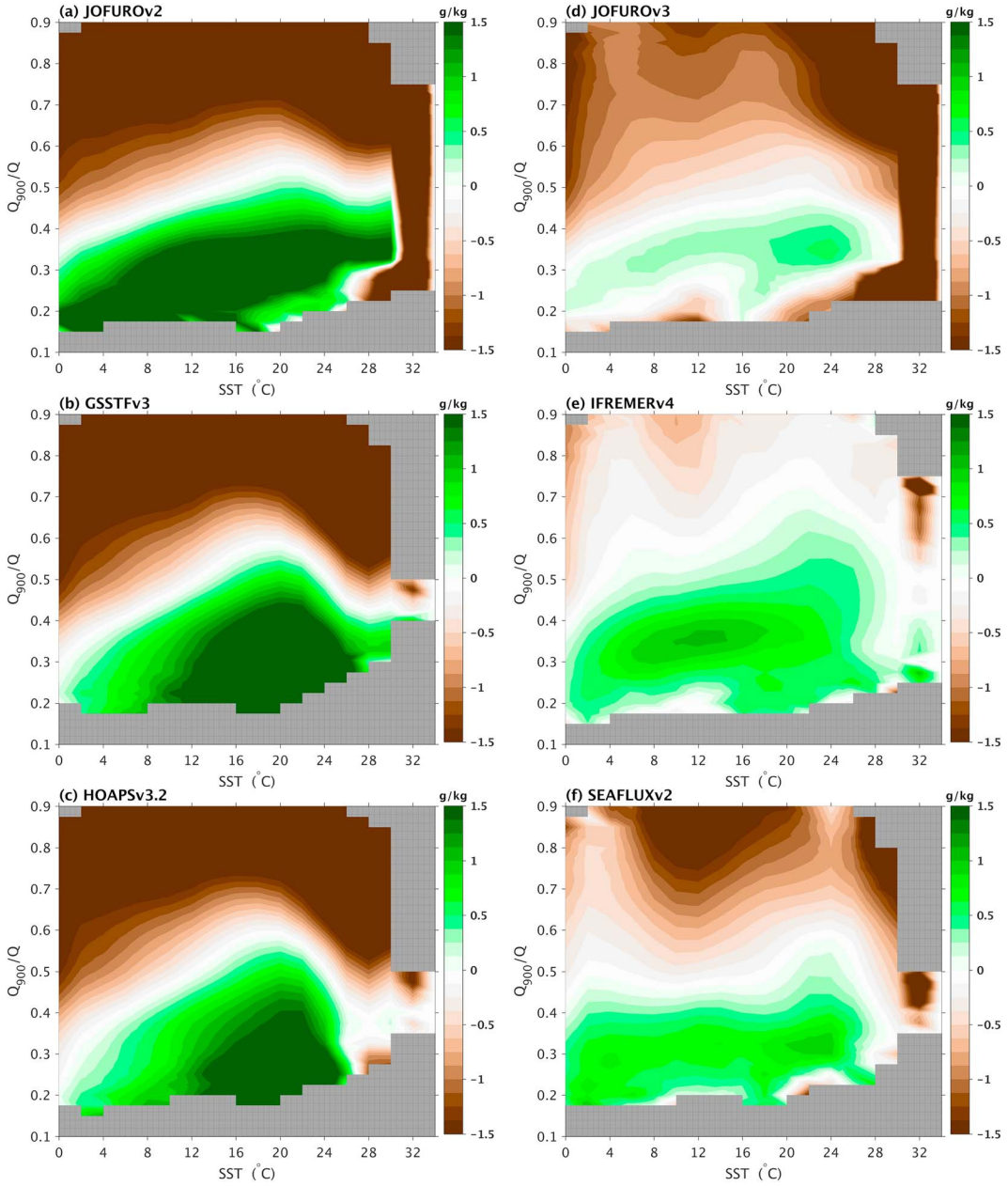

Figure 4. Composite binned mean differences are shown for (a) JOFUROv2, (b) GSSTFv3 (c) HOAPSv3.2, (d) JOFUROv3, (e) IFREMERv4, and (f) SEAFLUXv2 over the common period 1992–2008 within the two-parameter water vapor fraction versus sea surface temperature space. Products which only use brightness temperature observations as algorithm inputs are in the left panels while those including additional a priori inputs are organized in the right panels.
GSSTFv3 = Goddard Satellite-based Surface Turbulent Fluxes version 3; HOAPSv3.2 = Hamburg Ocean Atmosphere Parameters and Fluxes from Satellite version 3.2; IFREMERv4 = Institut Français pour la Recherche et l'Exploitation de la MER version 4; JOFUROv2 = Japanese Ocean Flux Data Sets with Use of Remote Sensing Observations version 2.

bias of 0.1–0.2 g/kg where lower layer moisture concentration is most peaked. However, the latter two products both show moist biases of 0.5 g/kg in strongly advective and convergent regions (A+C+). These occur primarily in the extratropical storm tracks and can be seen Figure 1.

It has been known since Liu (1986) that the strong connection between total columnar water vapor and surface layer specific humidity breaks down at shorter time scales; this was the impetus for Schulz et al. (1993) to isolate a boundary layer water vapor signal for use in *Q*air retrievals. Clearly, inclusion of a priori information on water vapor stratification as in JOFUOROv3 has the ability to sharply reduce, but not eliminate, the

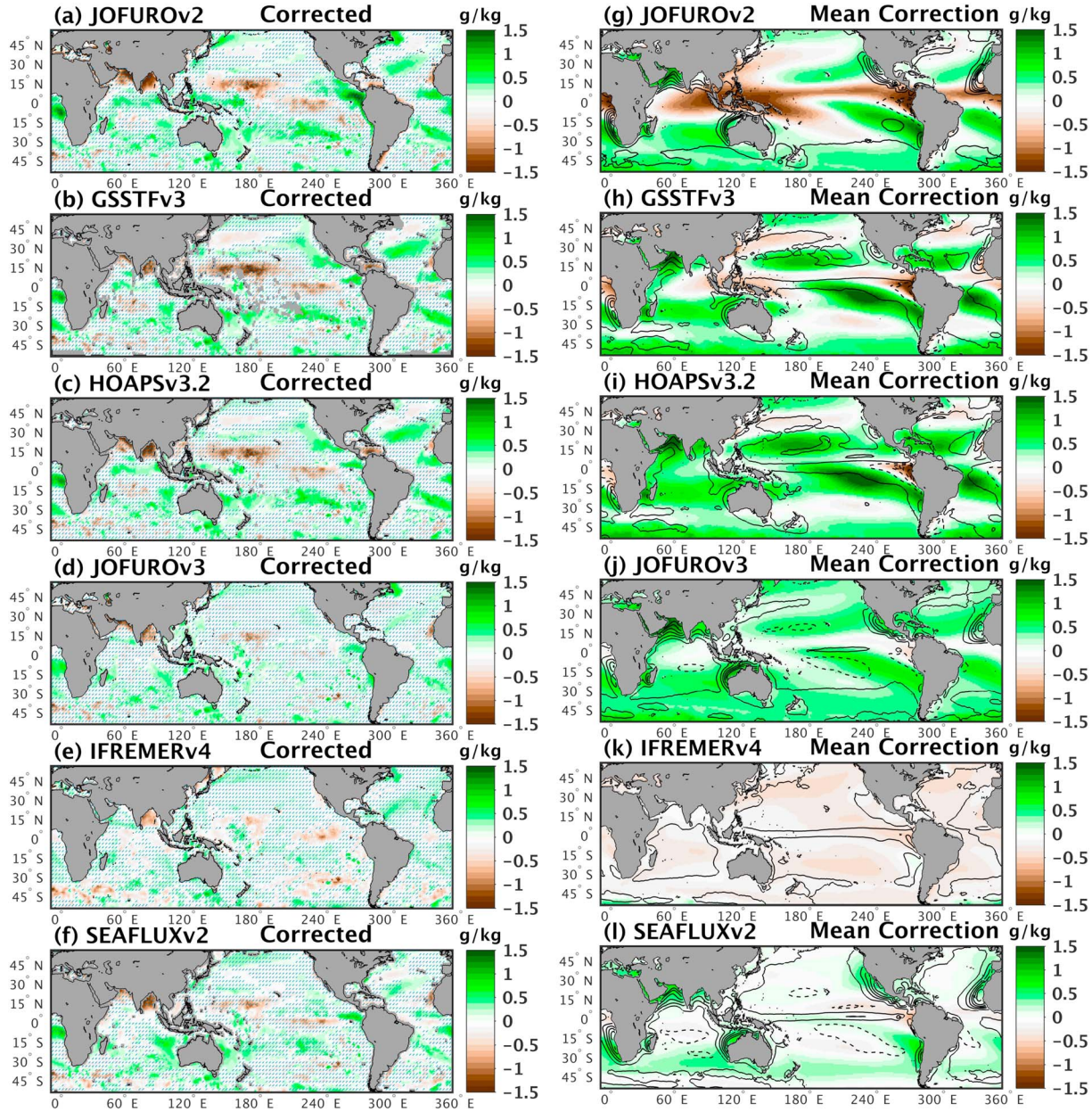

Figure 5. (a–f) Mean differences are shown after the implementation of a state-dependent bias correction for each product. Hatched regions indicate where the bias amplitude has been reduced. (g–l) The time-mean corrections are shown. Contours (0.1 g/kg; negative is dashed) indicate the difference between the three-parameter look-up table correction and a two-parameter (see text) correction. Positive contours thus indicate the three-parameter correction adding additional moisture. GSSTFv3 = Goddard Satellite-based Surface Turbulent Fluxes version 3; HOAPSv3.2 = Hamburg Ocean Atmosphere Parameters and Fluxes from Satellite version 3.2; IFREMERv4 = Institut Français pour la Recherche et l'Exploitation de la MER version 4; JOFUROv2 = Japanese Ocean Flux Data Sets with Use of Remote Sensing Observations version 2.

conditional biases related to moisture convergence. However, inclusion of SST information as in IFREMERv4 and SEAFLUXv2 also partially accounts for this bias; note that the regions of highest SSTs are typically collocated with the regions of deep convection and mixing. SSTs also provide information on average atmospheric temperature and humidity in a large-scale climatological sense (e.g., warm, wet tropics and cold, drier extratropics). In short, both water vapor stratification and SSTs provide additional independent constraints that help mitigate the underlying conditional biases.

In an attempt to better clarify these underlying relationships, Figure 4 provides an analysis of the retrieval biases as conditioned within the SST-$^{Q_{900}}/_{Q}$ space. Errors have been stratified using the same axis

Table 2
Bias Statistics Before and After Correction

Product	|Original bias| (g/kg)[a]	|Corrected bias| (g/kg)[a]	Percent with reduced bias (%)	Mean reduction (g/kg)	Mean amplification (g/kg)
JOFUROv2	0.54	0.26	89	0.50	0.17
JOFUROv3	0.43	0.18	95	0.35	0.14
GSSTFv3	0.60	0.26	92	0.55	0.16
IFREMERv4	0.30	0.18	92	0.25	0.19
HOAPSv3.2	0.53	0.25	90	0.49	0.15
SEAFLUXv2	0.28	0.20	86	0.21	0.07

Note. GSSTFv3 = Goddard Satellite-based Surface Turbulent Fluxes version 3; HOAPSv3.2 = Hamburg Ocean Atmosphere Parameters and Fluxes from Satellite version 3.2; IFREMERv4 = Institut Français pour la Recherche et l'Exploitation de la MER version 4; JOFUROv2 = Japanese Ocean Flux Data Sets with Use of Remote Sensing Observations version 2.
[a]These values represent the mean of the absolute value of the biases for all ocean pixels.

partitioning discussed in section 3.2 for these variables. For the older, TB-only retrieval algorithms, strong gradients of the biases are present along both axes. The most prominent bias gradient is that related to the water vapor stratification with moist biases being present in conditions associated with deeply mixed (i.e., low $^{Q_{900}}/_{Q}$) conditions and dry biases in environments with strong boundary layer moisture concentration. For more well mixed atmospheres, there is also an increase in the moist bias with increasing SST. The newer retrieval algorithms that incorporate a priori information appear to mitigate these biases found in the TB-only algorithms. JOFUROv3, which uses water-vapor-scale-height-dependent regressions but not SST information, strongly reduces the bias gradient along the water vapor fraction axis, as one might expect. SEAFLUXv2, which incorporates SST as an input but lacks information on water vapor stratification, reduces the gradient along the SST axis but maintains a prominent—albeit reduced from TB-only—bias gradient associated with water vapor fraction. IFREMERv4 represents an algorithm that incorporates a priori information on the SST and the near-surface stability. It is seen that both the biases along the SST and water vapor stratification axis are reduced though a moist bias of 0.5 g/kg is found for moderate SSTs and well-mixed atmospheres; these are likely associated with extratropical frontal systems. Though not shown, a weak dependence on the LWP was also found in similarly binned diagrams. It has been shown in studies such as Roberts et al. (2010) that cloud liquid water can mask water vapor emission signals leading to *Q*air biases. Referring back to Figure 2, it is clear that the large-scale dynamical regimes are important for controlling the distribution of water vapor stratification and cloudiness. We find that Figures 2–4 clearly demonstrate the connection of retrieval biases due principally to conditional biases in water vapor stratification and SST to the coherent bias patterns shown in Figure 1. That is, water vapor transport dynamics are tightly linked to water vapor stratification and cloudiness that result in biases of *Q*air estimates stemming from the limited information on these conditions within the brightness temperature observations alone. More recent algorithms that specify this type of information (i.e., JOFUROv3, SEAFLUXv2, and IFREMERv4) appear to reduce, though not eliminate these conditional biases. However, none of these latter algorithms include explicit information on water vapor stratification, cloudiness, and SSTs simultaneously.

To show the value of this additional information, we have developed a bias correction through development of a three-dimensional look-up table for each product based on the MERRA-2 water vapor fraction, SST, and LWP. For each day of observations, we used the observed MERRA-2 parameters to estimate the state-dependent satellite product biases (and hence required correction) at each grid point through trilinear interpolation of a look-up table described in section 3.2. Figure 5 demonstrates the new, reduced systematic errors for each product in addition to the long-term mean correction. Hatched regions indicate those areas where the amplitude of the bias has been reduced from the original data. Table 2 provides statistics for each product on the average bias amplitude before and after correction, the percentage of points with a reduced bias amplitude, and the average correction for points with a reduced or amplified bias strength. As expected, all products have a reduced bias amplitude on average, with all but SEAFLUXv2 (86%) exhibiting bias reductions for approximately 90% or more of the global ocean pixels. For those locations exhibiting bias reductions, the TB-only algorithms exhibit approximately 0.5-g/kg bias reductions, while the more recent algorithms are approximately 0.2–0.3 g/kg. For the small fraction of locations (~10%) where biases are amplified, the adjustments are all below 0.2 g/kg.

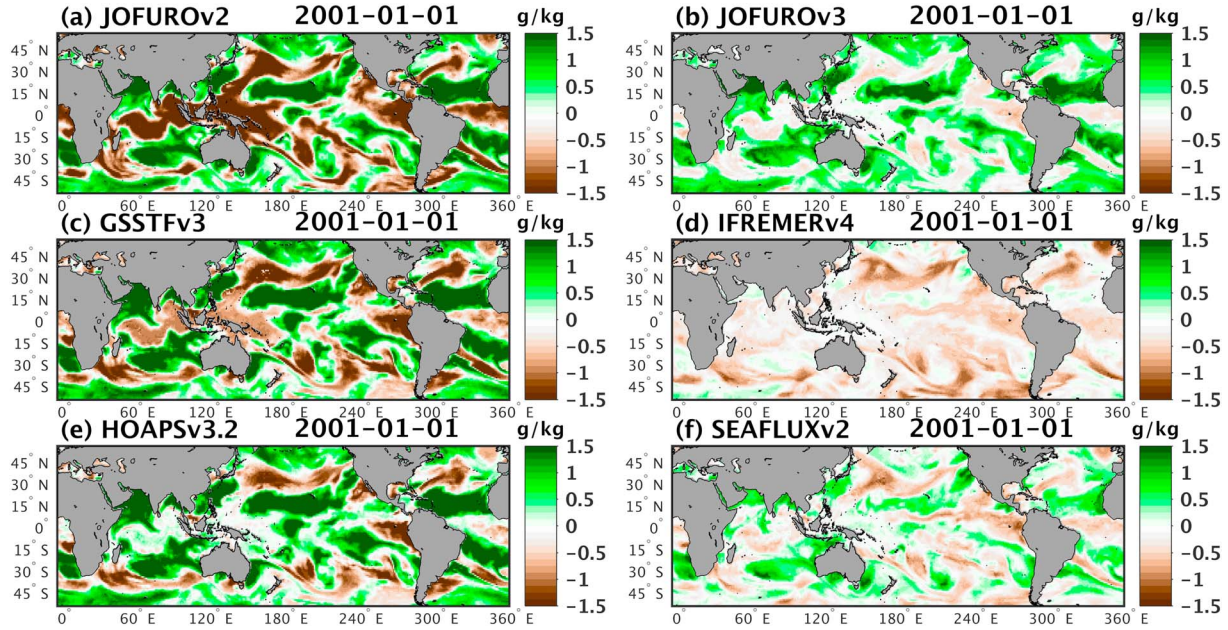

Figure 6. (a–f) The daily resolution corrections for a single day, 1 January 2001, are shown to illustrate the typical character of the correction for each product. Note the strong synoptic scale organization and the larger corrections for temperature-only algorithms. GSSTFv3 = Goddard Satellite-based Surface Turbulent Fluxes version 3; HOAPSv3.2 = Hamburg Ocean Atmosphere Parameters and Fluxes from Satellite version 3.2; IFREMERv4 = Institut Français pour la Recherche et l'Exploitation de la MER version 4; JOFUROv2 = Japanese Ocean Flux Data Sets with Use of Remote Sensing Observations version 2.

Figures 5a–5f illustrate the spatial pattern of bias after correction and can be contrasted with those in Figure 1. Figures 5g–5l depict the time-mean correction patterns as well as the additional correction provided by including LWP as an independent parameter. The TB-only-based estimates, seen in Figures 5a–5c, show substantially reduced biases overall though a dry bias of up to 0.5 g/kg appears to remains over the northwestern equatorial Pacific, Bay of Bengal, and the Arabian Sea. The time-mean correction patterns closely mirror the bias patterns found in Figure 1. Contours in Figures 5g–5l indicate additional moistening over the northern Indian Ocean (up to 0.5 g/kg) that are in excess of corrections using only a two-dimensional water vapor fraction and SST correction without LWP data. The added contributions from LWP information are a smaller-order (generally 0.1–0.2 g/kg) correction compared to the time-mean corrections exceeding 1 g/kg for TB-only products; but for the more recent products where biases are smaller, additional information from the LWP correction are more significant and can approach 30–50% of the total correction. Those algorithms including a priori information (see Figures 5d–5f and 5j–5l) now exhibit very small biases across the global oceans with limited coherent signatures.

For completeness, Figures 6 demonstrates the large-scale coherence of the corrections at daily resolution. The patterns are more muted for those products incorporating a priori information; however, all corrections exhibit large-scale organization on the synoptic scale; these are driven primarily by the patterns of water vapor convergence/divergence. Figure 7 illustrates the open ocean (55°N to 55°S) area-average time series of surface humidity before and after corrections are implemented. As Kent et al. (2014) find, annual mean differences greater than 0.5 g/kg are found between the original product estimates. Both IFREMERv4 and SEAFLUXv2 represent an upper range on the estimates while most of the TB-only estimates are relatively drier by 0.3–0.5 g/kg. Consistent with the weak dry bias in Figure 1, JOFUROv3 is drier compared to surface observations and falls below JOFUROv2 and toward the lower range of estimates that include HOAPSv3.2 and GSSTFv3, which exhibit significant (greater than 1.25 g/kg) dry biases in the subtropical trade-inversion regime. Obviously, there are compensating regional biases over this areal mean for the latter products. After corrections, all estimates collapse to within about 0.2 g/kg of one another in the areal mean after 2000 with consistent seasonal cycle amplitudes. In this sense, total uncertainties in the areal mean are reduced by up to 50% and are approaching the 0.2 g/kg stated mean uncertainties in the surface observations (Berry & Kent, 2011). In the early to mid-1990s, the spread is also reduced by about 50% but only to about 0.4 g/kg. During

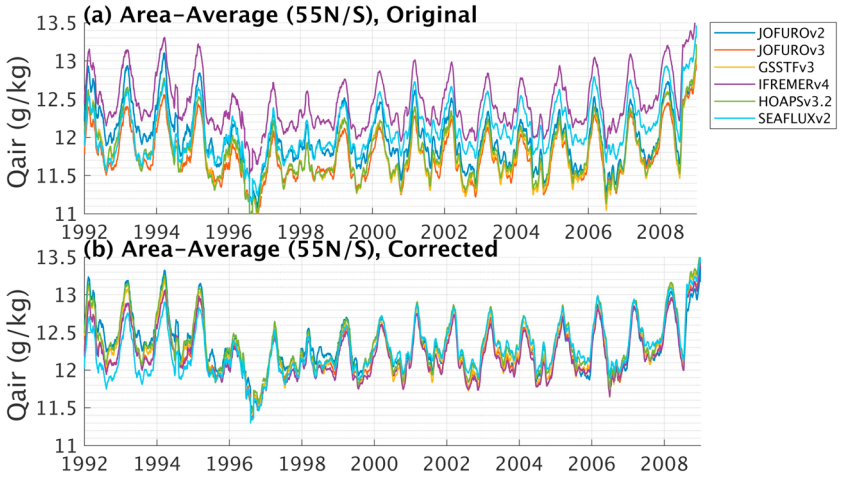

Figure 7. Ocean area-average (55°N to 55°S) *Q*air time series are shown for all six product estimates for the (a) original and (b) bias-corrected data. Samples are only included in the computations when all products are simultaneously available thus eliminating differences that arise due to sampling variability (e.g., use of different cloud/rain masks). GSSTFv3 = Goddard Satellite-based Surface Turbulent Fluxes version 3; HOAPSv3.2 = Hamburg Ocean Atmosphere Parameters and Fluxes from Satellite version 3.2; IFREMERv4 = Institut Français pour la Recherche et l'Exploitation de la MER version 4; JOFUROv2 = Japanese Ocean Flux Data Sets with Use of Remote Sensing Observations version 2.

this time frame, there are fewer microwave radiometers available and intersensor calibration, interpolation procedures, and other factors are likely also impacting product uncertainties.

5. Conclusions

The results presented in this study indicate a strong relationship between observed *Q*air biases and dynamical regimes of moisture convergence/divergence resulting in specific characteristics of water vapor stratification and cloudiness regimes. The large-scale coherence of systematic errors in *Q*air from passive microwave-based satellite retrievals are an imprint of conditional dependencies upon water vapor stratification, cloud effects, and SSTs that are organized through the large-scale dynamics. Because the relationship between near-surface and total columnar humidity is linked to water vapor dynamics, the use of statistical regressions that are essentially unconditioned upon this factor will either overpredict or underpredict the near-surface humidity as one deviates from the "typical" water vapor stratification resolved by the training data used in the statistical regressions; that is, a conditional bias remains. It has been shown that a simple a posteriori bias correction conditioned on these parameters significantly reduces the interproduct differences resulting in more consistent and accurate—relative to surface observations—representations of surface humidity. However, some residual biases remain and it is likely that proper inclusion of these additional conditional dependencies should be undertaken at the retrieval level itself as done in Tomita et al. (2018) for the development of JOFUROv3. The need for more accurate a priori information on vertical stratification is also supported by studies such as Jackson et al. (2006) who demonstrate using microwave imager observations together with direct information from microwave sounders significantly improves retrievals of *Q*air. However, multisensor-based retrievals as in Jackson et al. (2006) tend to have significantly reduced sampling as collocated observations from separate sensors are required. It should be noted that as more a priori information is added as part of the algorithm retrieval itself, the surface humidity estimates will themselves become less independent from sources of that information. Use of reanalysis information to specify water vapor stratification, for example, could introduce errors related to those in the reanalysis itself. The necessary inclusion of this information stems from the lack of significant direct sensitivities to water vapor stratification and SST (Special Sensor Microwave/Imager does not contain 6- or 10-GHz channel) in the traditional set of microwave imagers applied to problems of over-ocean *Q*air estimation. Future development efforts in this area should include (i) physically based variational estimates that incorporate background information in a consistent framework and (ii) application of multisensor retrievals that incorporate additional temperature and humidity information from the boundary layer. Finally, the spatial coherence of

the large-scale biases—even at the instantaneous level—indicates that any optimal estimation-based analyses must treat observational error covariance structures with care.

Acknowledgments
Data products used in this study are made publicly available via multiple repositories hosted by individual data product producers. JOFUROv2 and JOFUROv3 data are available online (https://j-ofuro.scc.u-tokai.ac.jp/en/). IFREMERv4 and NOCS surface data are available through the OceanHeatFlux project (https://www.ifremer.fr/oceanheatflux/Data). GSSTFv3 (doi:10.5067/MEASURES/GSSTF/DATA301) and MERRA-2 data are obtained from the Goddard Earth Sciences Data and Information Services Center. HOAPSv3.2 data are available from Satellite Application Facility on Climate Monitoring (https://doi.org/10.5676/EUM_SAF_CM/HOAPS/V001). SEAFLUXv2 data are accessed through the National Centers for Environmental Information (http://doi.org/10.7289/V59K4885). Daily surface observations were provided by David Berry and Elizabeth Kent. This work is supported under the NASA Physical Oceanography Program Grant NNX14AK48A.

References

Andersson, A., Fennig, K., Klepp, C., Bakan, S., Grasl, H., & Schulz, J. (2010). The Hamburg Ocean Atmosphere Parameters and Fluxes from Satellite Data—HOAPS-3. *Earth System Science Data*, *2*(2), 215–234. https://doi.org/10.5194/essd-2-215-2010

Bentamy, A., Grodsky, S. A., Katsaros, K., Mestas-Nunez, A. M., Blanke, B., & Desbiolles, F. (2013). Improvement in air-sea flux estimates derived from satellite observations. *International Journal of Remote Sensing*, *4*(14), 237–285. https://doi.org/10.1613/jair.301

Bentamy, A., Katsaros, K. B., Mestas-Nuñez, A. M., Drennan, W. M., Forde, E. B., & Roquet, H. (2003). Satellite estimates of wind speed and latent heat flux over the global oceans. *Journal of Climate*, *16*(4), 637–656. https://doi.org/10.1175/1520-0442(2003)016<0637:SEOWSA>2.0.CO;2

Bentamy, A., Piollé, J. F., Grouazel, A., Danielson, R., Gulev, S., Paul, F., et al. (2017). Review and assessment of latent and sensible heat flux accuracy over the global oceans. *Remote Sensing of Environment*, *201*(July), 196–218. https://doi.org/10.1016/j.rse.2017.08.016

Berry, D. I., & Kent, E. C. (2009). A new air–sea interaction gridded dataset from ICOADS with uncertainty estimates. *Bulletin of the American Meteorological Society*, *90*(5), 645–656. https://doi.org/10.1175/2008BAMS2639.1

Berry, D. I., & Kent, E. C. (2011). Air-Sea fluxes from ICOADS: The construction of a new gridded dataset with uncertainty estimates. *International Journal of Climatology*, *31*(7), 987–1001. https://doi.org/10.1002/joc.2059

Berry, D. I., & Kent, E. C. (2016). Assessing the health of the in situ global surface marine climate observing system. *International Journal of Climatology*, *37*(5), 2248–2259. https://doi.org/10.1002/joc.4914

Brunke, M. a., Wang, Z., Zeng, X., Bosilovich, M., & Shie, C.-L. (2011). An assessment of the uncertainties in ocean surface turbulent fluxes in 11 reanalysis, satellite-derived, and combined global datasets. *Journal of Climate*, *24*(21), 5469–5493. https://doi.org/10.1175/2011JCLI4223.1

Chou, S.-H., Atlas, R. M., Shie, C.-L., & Ardizzone, J. (1995). Estimates of surface humidity and latent heat fluxes over oceans from SSM/I data. *Monthly Weather Review*, *123*(8), 2405–2425. https://doi.org/10.1175/1520-0493(1995)123<2405:EOSHAL>2.0.CO;2

Chou, S.-H., Shie, C.-L., Atlas, R. M., & Ardizzone, J. (1997). Air-sea fluxes retrieved from SSM/I data. *Journal of Geophysical Research*, *102*(C6), 12,706–12,726, June 15, 1997. https://doi.org/10.1029/97JC00978

Clayson, C. A. (2016). Ocean surface bundle—Climate Algorithm Theoretical Basis Document, NOAA Climate Data Record Program [CDRP-ATBD-0578] Rev. 2 (2016). Available at https://www.ncdc.noaa.gov/cdr/

Fairall, C. W., Bradley, E. F., Hare, J. E., Grachev, A. A., & Edson, J. B. (2003). Bulk parameterization of air sea fluxes: Updates and verification for the COARE algorithm. *Journal of Climate*, *16*(4), 571–591. https://doi.org/10.1175/1520-0442(2003)016<0571:BPOASF>2.0.CO;2

Gelaro, R., McCarty, W., Suárez, M. J., Todling, R., Molod, A., Takacs, L., et al. (2017). The Modern-Era Retrospective Analysis for Research and Applications, Version 2 (MERRA-2). *Journal of Climate*, *30*(14), 5419–5454. https://doi.org/10.1175/JCLI-D-16-0758.1

Gulev, S., Jung, T., & Ruprecht, E. (2007). Estimation of the impact of sampling errors in the VOS observations on air sea fluxes. Part I: Uncertainties in climate means. *Journal of Climate*, *20*(2), 279–301. https://doi.org/10.1175/JCLI4010.1

Jackson, D. L., & Wick, G. A. (2010). Near-surface air temperature retrieval derived from AMSU-A and sea surface temperature observations. *Journal of Atmospheric and Oceanic Technology*, *27*(10), 1769–1776. https://doi.org/10.1175/2010jtecha1414.1

Jackson, D. L., Wick, G. A., & Bates, J. J. (2006). Near-surface retrieval of air temperature and specific humidity using multisensor microwave satellite observations. *Journal of Geophysical Research*, *111*, 1–16. https://doi.org/10.1029/2005JD006431

Jones, P. W. (1999). First- and second-order conservative remapping schemes for grids in spherical coordinates. *Monthly Weather Review*, *127*(9), 2204–2210. https://doi.org/10.1175/1520-0493(1999)127<2204:FASOCR>2.0.CO;2

Josey, S. A., Yu, L., Gulev, S., Jin, X., Tilinina, N., Barnier, B., & Brodeau, L. (2014). Unexpected impacts of the tropical Pacific array on reanalysis surface meteorology and heat fluxes. *Geophysical Research Letters*, *41*, 6213–6220. https://doi.org/10.1002/2014GL061302

Kent, E. C., Berry, D. I., Prytherch, J., & Roberts, J. B. (2014). A comparison of global marine surface-specific humidity datasets from in situ observations and atmospheric reanalysis. *International Journal of Climatology*, *34*(2), 355–376. https://doi.org/10.1002/joc.3691

Large, W. G., & Pond, S. (1982). Sensible and latent heat flux measurements over the ocean. *Journal of Physical Oceanography*, *12*(5), 464–482. https://doi.org/10.1175/1520-0485(1982)012<0464:SALHFM>2.0.CO;2

L'Ecuyer, T. S., Beaudoing, H. K., Rodell, M., Olson, W., Line, B., Kato, S., et al. (2015). The observed state of the energy budget in the early twenty-first century. *Journal of Climate*, *28*(21), 8319–8346. https://doi.org/10.1175/JCLI-D-14-00556.1

Liu, W. T. (1986). Statistical relation between monthly mean precipitable water and surface-level humidity over global oceans. *Monthly Weather Review*, *114*(8), 1591–1602. https://doi.org/10.1175/1520-0493(1986)114<1591:SRBMMP>2.0.CO;2

Prytherch, J., Kent, E. C., Fangohr, S., & Berry, D. I. (2014). A comparison of SSM/I-derived global marine surface-specific humidity datasets. *International Journal of Climatology*, *35*(9), 2359–2381. https://doi.org/10.1002/joc.4150

Roberts, J. B., Clayson, C. A., Robertson, F. R., & Jackson, D. L. (2010). Predicting near-surface atmospheric variables from Special Sensor Microwave/Imager using neural networks with a first-guess approach. *Journal of Geophysical Research*, *115*. https://doi.org/10.1029/2009JD013099

Roberts, J. B., Robertson, F. R., Clayson, C. A., & Bosilovich, M. G. (2012). Characterization of turbulent latent and sensible heat flux exchange between the atmosphere and ocean in MERRA. *Journal of Climate*, *25*(3), 821–838. https://doi.org/10.1175/JCLI-D-11-00029.1

Robertson, F. R., Bosilovich, M. G., Roberts, J. B., Reichle, R. H., Adler, R., Ricciardulli, L., et al. (2014). Consistency of estimated global water cycle variations over the satellite era. *Journal of Climate*, *27*(16), 6135–6154. https://doi.org/10.1175/JCLI-D-13-00384.1

Rodell, M., Beaudoing, H. K., L'Ecuyer, T. S., Olson, W. S., Famiglietti, J. S., Houser, P. R., et al. (2015). The observed state of the water cycle in the early twenty-first century. *Journal of Climate*, *28*(21), 8289–8318. https://doi.org/10.1175/JCLI-D-14-00555.1

Schlüssel, P., Schanz, L., & Englisch, G. (1995). Retrieval of latent heat flux and longwave irradiance at the sea surface from SSM/I and AVHRR measurements. *Advances in Space Research*, *16*(10), 107–116. https://doi.org/10.1016/0273-1177(95)00389-V

Schulz, J., Schluessel, P., & Grassl, H. (1993). Water vapour in the atmospheric boundary layer over oceans from SSM/I measurements. *International Journal of Remote Sensing*, *14*(15), 2773–2789. https://doi.org/10.1080/01431169308904308

Shie, C.-L. (2014). Science background for the reprocessing and Goddard Satellite-based Surface Turbulent Fluxes (GSSTF3) data set for global water and energy cycle research, Science Document for the Distributed GSSTF3 via Goddard Earth Sciences (GES) Data and Information Services Center (DISC) (21 pp.). (Available online at: https://docserver.gesdisc.eosdis.nasa.gov/public/project/MEaSUREs/GSSTF/Science_of_the_data.GSSTF3.pdf)

Tomita, H., Hihara, T., & Kubota, M. (2018). Improved satellite estimation of near-surface humidity using vertical water vapor profile information. *Geophysical Research Letters*, *45*(2), 899–906. https://doi.org/10.1002/2017GL076384

Tomita, H., Kubota, M., Cronin, M. F., Iwasaki, S., Konda, M., & Ichikawa, H. (2010). An assessment of surface heat fluxes from J-OFURO2 at the KEO and JKEO sites. *Journal of Geophysical Research*, *115*, C03018. https://doi.org/10.1029/2009JC005545

Wentz, F. J. (1997). A well-calibrated ocean algorithm for SSM/I. *Journal of Geophysical Research*, *102*(C4), 8703–8718. https://doi.org/10.1029/96JC01751

Wong, S., & Behrangi, A. (2018). Regime-dependent differences in surface freshwater exchange estimates over the ocean. *Geophysical Research Letters*, *45*, 955–963. https://doi.org/10.1002/2017GL075567

Wong, S., Del Genio, A. D., Wang, T., Kahn, B. H., Fetzer, E. J., & L'Ecuyer, T. S. (2016). Responses of tropical ocean clouds and precipitation to the large-scale circulation: Atmospheric-water-budget-related phase space and dynamical regimes. *Journal of Climate*, *29*(19), 7127–7143. https://doi.org/10.1175/JCLI-D-15-0712.1